

Characterization of the Edge Crack Torsion (ECT) Test for Mode III Fracture Toughness Measurement of Laminated Composites.

James G. Ratcliffe
National Research Council
NASA Langley Research Center Hampton, VA 23681

ABSTRACT: The edge crack torsion (ECT) test is designed to initiate mode III delamination growth in composite laminates. An ECT specimen is a rectangular laminate, containing an edge delamination at the laminate mid-plane. Torsion load is applied to the specimens, resulting in relative transverse shear sliding of the delaminated faces. The test data reduction schemes are intended to yield initiation values of critical mode III strain energy release rate, G_{IIIc} , that are constant with delamination length. The test has undergone several design changes during its development. The objective of this paper was to determine the suitability of the current ECT test design as a mode III fracture test. To this end, ECT tests were conducted on specimens manufactured from IM7/8552 and specimens made from S2/8552 tape laminates. Several specimens, each with different delamination lengths are tested. Detailed, three-dimensional finite element analyses of the specimens were performed. The analysis results were used to calculate the distribution of mode I, mode II, and mode III strain energy release rate along the delamination front. The results indicated that mode III-dominated delamination growth would be initiated from the specimen center. However, in specimens of both material types, the measured values of G_{IIIc} exhibited significant dependence on delamination length. Furthermore, there was a large amount of scatter in the data. Load-displacement response of the specimens exhibited significant deviation from linearity before specimen failure. X-radiographs of a sample of specimens revealed that damage was initiated in the specimens prior to failure. Further inspection of the failure surfaces is required to identify the damage and determine that mode III delamination is initiated in the specimens.

Glossary of Terms

a	Insert length.
A	Constant from relation between stiffness and normalized insert length.
b	ECT specimen width.
B	Delamination front element length in x-direction.
C_{fr}	Test compliance.
C_{spc}	ECT specimen compliance.
C_{sub}	Sublamine compliance.
\bar{C}_{sub}	Average sublamine compliance.
C_{sys}	System compliance.
\square	Cross-head displacement.
$\square a$	Delamination front element length in y-direction.
$\square A$	Virtual area.
E_{11}	In-plane modulus along fiber direction.
E_{22}	In plane modulus perpendicular to fiber direction.
E_{33}	Transverse modulus.
G_{12}	In-plane shear modulus.
G_{13}	Transverse shear modulus.
G_{23}	Transverse shear modulus.
G_I	Mode I strain energy release rate.
G_{II}	Mode II strain energy release rate.
G_{III}	Mode III strain energy release rate.
G_{Ic}	Critical mode I strain energy release rate (initiation value).
G_{IIc}	Critical mode II strain energy release rate (initiation value).
G_{IIIc}	Critical mode III strain energy release rate (initiation value).
G_T	Total strain energy release rate.
\bar{G}_T	Average total strain energy release rate.
h_A	Thickness of Sublamine. A.
h_B	Thickness of Sublamine. B.
l	Distance separating load and support points along ECT specimen length.
L	ECT specimen length.
m	Constant from relation between stiffness and normalized insert length.
P	Applied load.
P_c^{max}	Maximum test load.
P_c^{NL}	Load at onset of non-linearity.
$P_c^{5\%}$	Load at intersection of 5% offset curve and load displacement response.
u_{Li}	Delamination front node displacement in X-direction, column L, row i.
v_{Li}	Delamination front node displacement in Y-direction, column L, row i.
W	Distance separating load and support pins along specimen width.
w_{Li}	Delamination front node displacement in Z-direction, column L, row i.
X_{Li}	X-direction delamination front force in column L, row i.
Y_{Li}	Y-direction delamination front force in column L, row i.
Z_{Li}	Z-direction delamination front force in column L, row i.

Introduction

Fiber reinforced composite materials are susceptible to delamination due to out-of-plane and shear loads, yielding a reduction in structural integrity and therefore reduced service lifetime [1]. Delamination in a structural laminate may consist of the mode I (opening), mode II (sliding shear) and mode III (scissoring shear) components of strain energy release rate. Considerable attention has been paid to mode I and mixed mode I/II fracture, resulting in standard testing techniques for characterizing such fracture behavior [2-3 respectively]. Mode II delamination has received some attention with the development of the four point bend end-notch flexure test (4ENF) [4]. Recent work [5], however, indicates there are a number of problems with the test method, that need to be resolved prior to standardization.

Mode III delamination has received considerable attention in the research community. Several test techniques have been proposed for characterizing mode III delamination fracture, including a split cantilever beam [6] and a crack rail shear specimen [7]. A more comprehensive description of developed mode III test methods is given in work detailing an anti-clastic plate bend test for mode III fracture [8]. The most commonly investigated mode III fracture test method is the edge crack torsion (ECT) test [9], which is the main subject of this paper. An ECT specimen is a rectangular laminate of tape composite material, containing an edge delamination at the mid-plane of the specimen. Equal and opposite moment arms are applied to the specimen ends (indicated by arrows between w in Fig. 1). The applied moment arms generate a torsion load in the specimen, resulting in relative shear sliding of the delaminated faces as depicted in Fig. 1. The original specimen stacking sequence was $[90/(+45/-45)_n/(-45/+45)_n/90]_s$, with $n=3$ or 4 depending on the composite material used to manufacture the specimens. The orientation corresponds to the coordinate system depicted in Fig. 1. It is assumed that delamination growth takes place along the 90° direction at the $90^\circ/90^\circ$ ply interface, constituting mode III delamination.

The original ECT test fixture consisted of a load frame whereby the specimen was positioned between three support pins, and load was applied via a fourth pin, as illustrated in Fig. 2a. A number of studies concluded that this specimen produced mode III-dominated loading at the delamination front in the center of the specimen, away from the loading points [10-11]. A round robin exercise was organized by the ASTM D30 committee to characterize the test method [12]. The ECT tests were undertaken in five independent laboratories on specimens manufactured from the toughened carbon/epoxy system, HTA/6376. Large scatter in calculated fracture toughness values were reported, and some laboratories reported significant nonlinearity in load-displacement response of the specimens. Consequently, the test frame was modified, resulting in a symmetrical load application via two pins, as illustrated in Fig. 2b. A loading beam was used to allow uniform load transfer from test machine to the loading pins. Zero-degree plies were added to the specimen, yielding the stacking sequence $[90/0/(+45/-45)_n/(-45/+45)_n/0/90]_s$.

A second round-robin study involved ECT tests (using the modified specimen and test fixture) conducted on specimens manufactured from S2/8552 glass/epoxy tape and IM7/8552 carbon/epoxy tape [13]. Delaminations were found

to grow along the 90/0 interface in some glass/epoxy specimens, instead of along the intended 90/90 interface [13]. Additionally, it was shown that a significant mode II component of strain energy release rate, G_{II} , was generated near to the location of the loading pins [13]. It was argued that increasing the specimen length, L , would reduce this mode II component and therefore promote mode III delamination in the center portion of the specimen [13]. Consequently, the specimen length was increased from 82.5-mm to 108-mm.

The objective of this paper was to characterize the current ECT test method to determine its suitability for inducing mode III delamination growth. Tests were conducted on specimens manufactured from IM7/8552 and specimens made from S2/8552 tape laminates. Specimens with insert lengths (normalized by specimen width, b), a/b , of 0.2, 0.3, 0.4, 0.5, and 0.6 were tested. Two data reduction techniques were used to calculate the critical mode III strain energy release rates, G_{IIIc} .

A selection of specimens was also inspected using a dye-penetrant X-ray technique. Detailed, 3D finite element analyses of all specimens were conducted. Analysis results were used to calculate distribution of strain energy release rate components along the edge delamination front. Findings from the ECT tests and analysis were used to determine the suitability of the current data reduction methods for calculating G_{IIIc} .

Experimental Procedures

Specimen and Materials

An ECT specimen is a rectangular laminate of tape composite material, Fig. 1. Dimensions of the specimen are also provided in the figure. A 13- μ m-thick PTFE (Teflon[®]) insert was positioned at the mid-plane of the specimen to introduce an edge delamination crack. Stacking sequence of the specimen was a function of material used. Specimens manufactured from IM7/8552 carbon/epoxy tape had the stacking sequence, $[90/0(+45/-45)_2/(-45/+45)_2/0/90]_s$. Additional cross-plyies were added to specimens manufactured from S2/8552 glass/epoxy tape laminate, yielding the stacking sequence, $[90/0(+45/-45)_3/(-45/+45)_3/0/90]_s$. Ply orientations correspond to the coordinate system given in Fig. 1. The fiber volume fraction of the specimens was 60%. Specimens were cured in an autoclave using cure cycle suggested by the composite material manufacturer. All specimens were manufactured by Bell Helicopter Textron.

Specimens with five different insert lengths were manufactured and tested. The five normalized insert lengths, a/b , were 0.2, 0.3, 0.4, 0.5 and 0.6. Three repeat specimens of each insert length were tested, resulting in a total of 15 IM7/8552 ECT specimens and 15 S2/8552 ECT.

ECT Test Fixture

The load frame used for ECT testing is a symmetric two-point test fixture, Fig. 2b. Two support points are located diagonally to each other at the corners of

the test fixture. Two columns are located at the opposite corners to the support points. The columns contain vertical holes lined with spherical bearings. Specimens are placed onto the support points. Loading pins are placed through the holes in the columns, in order make contact with the specimen. The bearings lining the column holes reduce sliding friction between loading pin and the column. A loading beam is placed onto the loading pins, as illustrated in Fig. 2b. During an ECT test, load is applied at the center of the loading beam, in the direction indicated in Fig. 2b. The load is equally distributed to the ECT specimen through the load pins. Three guide pins are positioned on the fixture to enable precise specimen alignment. Two of these pins are visible in Fig. 2b. The third pin is hidden by the left-hand load-pin column.

ECT Tests

Prior to testing, all specimens were dried in an oven at 104°C for a 7-day period. Specimens were placed in a dessicator after the drying period and were tested within 1 day after removal from the oven.

Specimen dimensions were measured to the nearest 0.05mm. Measurements of the width (dimension b) were taken at the mid-point and at a distance 6.35 mm from each end in the y-direction (Fig. 1) resulting in three measurements. Measurements for the length (dimension L) were taken at the mid-point and at a distance 6.35 mm from each end in the x-direction, again resulting in three measurements. Measurement of the thickness were taken at the center of the specimen and at the intersections of the lines created a distance 6.35mm from each edge resulting in five measurements. All specimen dimensions were taken as the average of the corresponding measurements.

The ECT tests were conducted using a servo-hydraulic test machine. Specimens were placed into the ECT test fixture, such that contact was made with all three guide pins, ensuring precise specimen alignment. After being leveled, specimens were loaded under displacement control at a rate of 1.3mm/min until failure. Specimens were unloaded at a rate of 5mm/min. Applied load, P , and cross-head displacement, Δ (referred to as displacement in remainder of paper), were recorded during each test using data acquisition software on a computer connected to the test machine. A load-displacement response typical from tests on both material types is given in Fig. 3. In most specimens, failure was indicated by a sudden reduction in load (plot 1 in Fig. 3). The maximum load applied to each specimen, P_c^{max} was recorded. Additionally, the load corresponding to the onset of nonlinearity of the load-displacement response, P_c^{NL} , was calculated using the technique detailed in Appendix A. An illustration of the location of P_c^{max} and P_c^{NL} on the load-displacement response is given in Fig. 3. IM7/8552 specimens with the largest insert length ($a/b = 0.6$) exhibited stable failure, as illustrated by plot 2 in Fig. 3. In this case, a line with slope 5% less than the original load-displacement response was superimposed onto the plot. The load corresponding to the intersection of the two curves, $P_c^{5\%}$, was recorded instead of P_c^{max} .

The total specimen compliance, C_{fr} , following each ECT test was calculated by taking the reciprocal of the slope of the load-displacement plot, as illustrated in Fig. 3.

Specimens containing the two smallest insert lengths (a/b ratios 0.2 and 0.3) were split about the specimen mid-plane, creating two sublaminates, labeled A and B. The thickness of each sublaminate, h_A and h_B , was measured to the nearest 0.05mm. Each sublaminate was returned to the ECT test fixture and loaded under displacement control at a rate of 1.3mm/min to a load equal to the maximum value attained in the original test. Load and displacement were again recorded throughout the test. The total compliance of each sublaminate, C_{sub} , was then calculated following the same technique used for the intact ECT specimens. An average of the compliance of sublaminates A and B, \bar{C}_{sub} , was then calculated.

The system compliance (compliance of test machine and ECT load frame), C_{sys} , was measured by loading a steel block positioned in the ECT test frame, up to the maximum load observed during the ECT testing. Load and displacement were recorded and C_{sys} was taken as the reciprocal of the slope of the load-displacement response.

After testing, all ECT specimens were split about the mid-plane and the insert length was measured at three locations along the delamination front length. The insert length, a , was then taken as the average of the three measurements.

Two additional carbon/epoxy specimens with normalized insert lengths of 0.3 were tested. The specimens were loaded to a level higher than the values of P_c^{NL} observed in previous tests on duplicate specimens, but lower than the maximum load, P_c^{max} . The specimens were unloaded and held at a constant displacement when the load reached approximately half the maximum test load. To prepare for X-ray inspection, a zink-iodide-based dye penetrant was then applied to the delamination edges of both specimens, taking care not to spill any penetrant on the specimen surfaces. This process lasted approximately 1 minute. The specimens were then unloaded. The load-displacement response of the specimens was recorded and the technique described in Appendix A was used to confirm that P_c^{NL} had been reached.

Data Reduction Methods

Two data reduction schemes were used to calculate initiation values of the critical strain energy release rate, G_{IIIc} . The first data reduction method employed a multi-specimen compliance calibration procedure. The second technique utilized a closed-form solution for mode III strain energy release rate, which was derived from laminated plate theory (LPT) in a previous study [10].

Compliance Calibration Method

The compliance of each ECT specimen, C_{spc} , was calculated by subtracting the system compliance from the test compliance ($C_{spc} = C_{fr} - C_{sys}$). The stiffness ($1/C_{spc}$) of all fifteen specimens of each material type were then plotted on the same

graph as a function of normalized insert length, a/b . Linear regression analysis was performed to determine the constants, A and m of the following expression for specimen stiffness [9]:

$$\frac{1}{C_{spc}} = A[1 - m(a/b)] \quad (1)$$

Only the constant, m , was used in the data reduction.

The perceived critical strain energy release rate of each ECT specimen was calculated based on the maximum critical load, P_c^{max} , and the load corresponding to the onset of nonlinearity, P_c^{NL} using the following expressions [9]:

$$G_{IIIc}^{CC}(max) = \frac{mC_{spc}(P_c^{max})^2}{2lb[1 - m(a/b)]} \quad (2)$$

$$G_{IIIc}^{CC}(NL) = \frac{mC_{spc}(P_c^{NL})^2}{2lb[1 - m(a/b)]} \quad (3)$$

The superscript on the left hand side of Eqns. 2 and 3 denote compliance calibration. The parameter, l , is the distance separating the load pins along the specimen length and b is the specimen width, Fig. 1.

The perceived critical strain energy release rates, $G_{IIIc}^{CC}(max)$ and $G_{IIIc}^{CC}(NL)$, were then plotted as functions of normalized insert length, a/b . This was repeated for both materials tested. It is noted that the resulting critical strain energy release rate values correspond only to fracture initiation. Hence, fracture resistance effects such as fiber bridging should not be present. The values of $G_{IIIc}^{CC}(max)$ and $G_{IIIc}^{CC}(NL)$ should therefore be independent of insert length.

Laminated Plate Theory (LPT) Method

The perceived critical strain energy release rate of specimens with normalized insert lengths, a/b , of 0.2 and 0.3 were calculated using the LPT method. As with the compliance calibration technique, perceived critical strain energy release rates corresponding to P_c^{max} and P_c^{NL} were calculated for each specimen using the following expressions [10]:

$$G_{IIIc}^{LPT}(max) = \frac{3LC_{spc}(P_c^{max})^2}{l^2W(\bar{C}_{sub} - C_{sys})} \quad (4)$$

$$G_{IIIc}^{LPT}(NL) = \frac{3LC_{spc}(P_c^{NL})^2}{l^2W(\bar{C}_{sub} - C_{sys})} \quad (5)$$

The parameter L is the total ECT specimen length and W is the distance separating the load pins along the specimen width, Fig. 1.

The values of $G_{IIIc}^{LPT}(max)$ and $G_{IIIc}^{LPT}(NL)$ were then plotted as functions of normalized insert length, a/b . This was repeated for both materials tested. The values were superimposed onto the plots of $G_{IIIc}^{cc}(max)$ and $G_{IIIc}^{cc}(NL)$ versus a/b , providing a comparison of the values calculated using the two data reduction methods.

Dye-Penetrant X-Ray Imaging

X-radiographs were taken of the two carbon/epoxy ECT specimens, penetrated with ink-based dye, using a Pantak Seifert X-ray system. This was done to determine whether damage was initiated from the insert after P_c^{NL} but before the maximum load, P_c^{max} , was reached. Radiographs were taken along three sections of each specimen. The images were then stitched together using graphics post processing software, yielding complete images of both specimens.

Numerical Analysis

Finite Element Models

Three-dimensional finite element models were constructed of the IM7/8552 and S2/8552 ECT specimens. Specimens with each normalized insert length were modeled. A summary of the specimen dimensions is given in Fig. 1. The models were constructed using the commercial code, ABAQUS version 6.3. Solid, eight-node brick elements were used to represent the specimens. A composite layer option was used to represent specimen stacking sequence, whereby one layer of elements was used to represent one or more plies. In this case, the orthotropic ply properties were oriented according to the specimen stacking sequence. An image of a finite element model (showing displaced geometry) is given in Fig. 4, illustrating the stacking sequence of a carbon/epoxy specimen. The edge delamination was modeled by including elements with coincident nodes on the plane of the delamination. A fine mesh was used in the vicinity of the delamination front to accommodate for the rapid change in strain field. The element thickness at the delamination front (in the y and z-axes) was one ply thickness as illustrated in Fig. 4. A similar meshing technique was adopted during an analysis of a double cantilever beam specimen [14]. Contact elements were used at the edge delamination plane to prevent mesh interpenetration during the analysis. Relative sliding between points in the delamination region was assumed frictionless. A prescribed displacement in the z-axis was applied at nodes corresponding to the point of contact of the loading pins. The same displacement was prescribed to each model, therefore simulating displacement control used during actual ECT tests. Displacement values were chosen to ensure an elastic response from the specimens, which was 2-mm in all cases. Nodes positioned at the locations of the support pins were constrained from displacement in the z-axis to represent contact between

specimen and the pins. Nodes positioned at the locations where contact takes place between the specimen and the load frame guide pins, were constrained from displacement in the corresponding axes, as illustrated in Fig. 4. These boundary conditions acted to prevent rigid body motion during an analysis run. The orthotropic ply properties used to represent IM7/8552 and S2/8552 are presented in Table 1. Geometrically nonlinear analyses were performed to facilitate contact in the models.

The reaction loads at the nodes to which displacement was prescribed was calculated, and specimen compliance was then determined by dividing prescribed displacement by the sum of these reaction loads.

Virtual Crack Closure Technique

The virtual-crack-closure-technique (VCCT) [16] was used to calculate the mode I, mode II and mode III components of strain energy release rate (G_I , G_{II} and G_{III} respectively) along the delamination front in each finite element model. A previously developed ABAQUS user subroutine was used to perform the VCCT calculations [17]. The technique works on the principle that the change in stored elastic strain energy associated with a small extension of crack area is equal to the work done required to close the crack to its original length. In terms of a finite element model constructed from solid, 8-node brick elements, G_I , G_{II} and G_{III} were calculated using the following equations [18]:

$$G_I = \frac{1}{2\Delta A} Z_{Li} (w_{Li} - w_{Li}^*) \quad (6)$$

$$G_{II} = \frac{1}{2\Delta A} Y_{Li} (v_{Li} - v_{Li}^*) \quad (7)$$

$$G_{III} = \frac{1}{2\Delta A} X_{Li} (u_{Li} - u_{Li}^*) \quad (8)$$

Figure 5 contains an illustration of the delamination front elements typical in the finite element models of the ECT specimens. The area $\Delta A = \Delta a B$ as shown in Fig. 5, where ΔA is the virtual area closed, Δa is the length of the elements at the delamination front and B is their width. The subscript in Eqns. 6–8 denote rows and columns of nodes as seen in the top view of the delamination front elements in Fig. 5b. Capital letters indicate columns and lower case letters indicate rows. Hence, X_{Li} , Y_{Li} and Z_{Li} denote the forces at the delamination front in row i , column L . The corresponding displacements behind the delamination front at the top face of node row i , column L in the x, y and z axes are denoted by u_{Li} , v_{Li} and w_{Li} respectively. The displacements at the bottom face of node row i , column L are denoted by u_{Li}^* , v_{Li}^* and w_{Li}^* . All the forces and displacements are obtained from the finite element analyses with respect to the global coordinate system (x, y, z). As each analysis was geometrically nonlinear, the forces and displacements were resolved into the local coordinate system (x', y', z') using the technique detailed in

[17]. Equations 6-8 were then used to calculate G_I , G_{II} and G_{III} at every node located along the delamination front. The strain energy release rate values were then plotted as a function of location along the delamination front, x/L .

The total strain energy release rate at any location along the delamination front, G_T , was calculated as the sum of the individual strain energy release rate components:

$$G_T = G_I + G_{II} + G_{III} \quad (9)$$

The total average strain energy release rate across the entire delamination length, \bar{G}_T , was computed as the integral of the total strain energy release rate divided by the delamination length.

Results and Discussion

Numerical Analysis Results

Finite Element Model Verification

The compliance of each ECT specimen, C_{spec} , was estimated from the finite element models and plotted as a function of normalized insert length. Figure 6 presents specimen stiffness versus normalized delamination length, a/b , calculated from the finite element models of the IM7/8552 ECT specimens. Included in the figure is a plot of specimen stiffness measured from the corresponding ECT tests. The constants A and m of Eqn. 1 were calculated using the finite element analyses and experimental data. Analysis and measured stiffness values agree to within 5%, indicating the analyses accurately captured the elastic response of the specimens. A similar comparison was made from the finite element analyses of the S2/8552 ECT specimens. Stiffness versus normalized insert length of these specimens is also given in Fig. 6. Again, plots from analysis and experiment are included for comparison. For the shorter insert lengths, $a/b = 0.2$ and 0.3 , the agreement between analysis and experiment is only within 10%, however, the agreement improves dramatically for the largest three insert lengths. Overall, the finite element models accurately captured the elastic response of the S2/8552 specimens.

Strain Energy Release Rate Distribution

Figure 7a contains plots of G_{II} and G_{III} versus distance along the delamination front computed from analyses of the IM7/8552 ECT specimens. The plots correspond to specimens with the smallest and largest normalized insert lengths, $a/b = 0.2$ and $a/b = 0.6$ respectively. The mode I strain energy release rate was found to be negligible in comparison to G_{II} and G_{III} for all specimens modeled, and is therefore not included in the plots of Fig. 7. For a given location along the delamination front, G_{II} and G_{III} , were found to decrease with increasing insert length. The strain energy release rate distribution is very similar to that reported from an analysis of the original ECT specimen [19] (Fig. 2a), with the exception that in the current analyses, the distribution was found to be symmetrical about the

specimen mid-length. The parameter, G_{II} , peaks at the locations of the load and support pins and G_{III} peaks along the center of the specimen. The load and support pins produce a moment arm that cause relative sliding of the delaminated sections of the specimen, parallel to the intended direction of delamination growth. Consequently, G_{II} is expected to peak at the location of the load pins. The finite element analyses were also used to calculate contact pressure in the region of the delamination. Contact pressure was negligible across most of the region, except at positions local to the load and support pins. Relative opening of the contact faces was also negligible. This supports the finding that G_I is negligible. It should be noted, however, that sliding friction of the delaminated surfaces was not considered. It was assumed that friction would not influence the strain energy release rate distribution along the delamination front.

In the case of all the IM7/8552 specimens, the peak value of G_{III} was approximately eight times the peak G_{II} value. Assuming $G_{IIIc} \geq G_{IIc}$, the above findings indicate that mode III-dominated delamination will initiate from the center of the specimen insert front.

Similar trends were found from analyses of S2/8552 ECT specimens, with the exception that G_{II} exhibited a slight increase with insert length, as illustrated in Fig. 7b. Again strain energy release rate distribution from analyses of specimens with smallest and largest insert lengths are presented in Fig. 7b. The results indicate that mode III-dominated delamination growth should take place from the center region of the specimen.

Effect of Insert Length on Average Total Strain Energy Release Rate

Figure 8 contains plots of average total strain energy release rate, \overline{G}_T , versus normalized insert length, calculated from analyses of the IM7/8552 and S2/8552 ECT specimens. In the case of the IM7/8552 specimens, \overline{G}_T decreases with insert length. Considering that the same displacement was prescribed in each analysis, the reduction in \overline{G}_T with insert length implies that delamination growth will be stable if testing is performed under displacement control. This result suggests that the use of P_c^{max} for calculating G_{IIIc} may be inaccurate, as delamination may occur prior to the sudden load drop that was observed during ECT tests. A similar trend was predicted for the S2/8552 specimens, except that an initial increase in \overline{G}_T was predicted for an increase in normalized insert length from 0.2 to 0.3, as shown in Fig. 8.

Experimental Results

ECT Specimen Load-Displacement Response

A sample of experimentally-measured load-displacement responses from tests on IM7/8552 and S2/8552 specimens is presented in Figs. 9a and 9b respectively. The responses from specimens of the two material type were similar. A typical load-displacement plot consisted of an initial nonlinear response, corresponding to seating of the load and support pins on the specimens. This was

proceeded by a linear response, after which the load-displacement response deviated from linearity. In most cases, the load reached a peak value, followed by a sudden load drop that was assumed to correspond to specimen failure. The IM7/8552 specimens containing the largest insert length ($a/b = 0.6$) exhibited stable failure, shown by the gradual change in slope at the upper portion of the load-displacement response. In the case of the IM7/8552 specimens, the deviation from linearity, P_c^{NL} , ranged from 90% to 93% of the maximum load, P_c^{max} . The extent of deviation from linearity was found to increase with increasing insert length. The glass/epoxy specimens exhibited more exaggerated deviation from linearity, with P_c^{NL} ranging from 50% to 75% of P_c^{max} . Again the extent of deviation from linearity increased with insert length.

Critical Mode III Strain Energy Release Rate of IM7/8552 Specimens


The perceived critical mode III strain energy release rate was calculated using the compliance calibration method. A plot of specimen stiffness versus normalized insert length from tests on both material types is presented in Fig. 10. The plots of $1/C_{spc}$ versus a/b from specimens of both materials exhibit a linear fit, validating the relationship of Eqn. 1. The values of perceived critical mode III strain energy release rate were calculated using Eqns. 2 and 3. Figure 11a contains the plots of $G_{IIIc}^{CC}(max)$ and $G_{IIIc}^{CC}(NL)$ versus normalized insert length for the IM7/8552 specimens. The values of $G_{IIIc}^{CC}(max)$ and $G_{IIIc}^{CC}(NL)$ are in good agreement for the two smallest insert lengths. However, $G_{IIIc}^{CC}(max)$ begins to deviate from $G_{IIIc}^{CC}(NL)$ when $a/b \geq 0.3$, where the values of $G_{IIIc}^{CC}(max)$ begin to increase with a/b while $G_{IIIc}^{CC}(NL)$ remains relatively constant. The $G_{IIIc}^{CC}(NL)$ values exhibited significant scatter. Similar scatter was observed in data generated from ECT tests conducted on glass/epoxy specimens [20]. The findings imply that the values of $G_{IIIc}^{CC}(max)$ do not correspond to G_{IIIc} (of IM7/8552) over the largest three insert lengths. In theory, the values are representative of fracture initiation, and therefore the measured critical mode III strain energy release rate should be constant with insert length.

The perceived critical mode III strain energy release rates calculated using the laminated plate theory method (Eqns. 3 and 4) are also plotted in Fig. 11a. The values of $G_{IIIc}^{LPT}(NL)$ agree very well with the $G_{IIIc}^{CC}(NL)$ values for specimens with the two smallest insert lengths. Similarly, values of $G_{IIIc}^{LPT}(max)$ are in good agreement with $G_{IIIc}^{CC}(max)$.

Averages of $G_{IIIc}^{CC}(NL)$ and $G_{IIIc}^{CC}(max)$ were calculated and plotted on the column chart presented in Fig. 11b. An average value for the critical mode II strain energy release rate of IM7/8552 is also given in the plot for comparison. The mode II fracture data was measured from four point bend end-notch flexure tests conducted on IM7/8552 specimens [21]. Error bars correspond to one standard deviation above and below the average values represented by the columns. The average values are also printed at the top of each column. The column representing

G_{IIc} is an average of only three data points, so caution is taken as to the statistical significance of the value. In all cases, scatter in the data is high, resulting in overlap of the $G_{IIIc}^{CC}(max$ and G_{IIc} values. The average value of $G_{IIIc}^{CC}(NL)$ is 17% lower than the average G_{IIc} . It is expected that G_{IIIc} should be equal to or greater than G_{IIc} . Hence, even though $G_{IIIc}^{CC}(NL)$ appears consistent with insert length, this value also may not be representative of G_{IIIc} .

Critical Mode III Strain Energy Release Rate of S2/8552 Specimens

Figure 12a contains plots of $G_{IIIc}^{CC}(NL)$, $G_{IIIc}^{CC}(max$,  and $G_{IIIc}^{LPT}(max$ measured from tests on the S2/8552 ECT specimens. Again, the values of $G_{IIIc}^{CC}(max$ increase with insert length, indicating the data is not representative of G_{IIIc} . The values of $G_{IIIc}^{CC}(NL)$ remain relatively constant with insert length. There is a greater difference between $G_{IIIc}^{CC}(NL)$ and $G_{IIIc}^{CC}(max$ in comparison to the IM7/8552 values. This is because the glass/epoxy specimens exhibited significantly more deviation from linearity before failure. There is also a significant difference between fracture data calculated using the laminated plate theory method and those values found from compliance calibration. Reasons for this difference are not understood, although they may be associated with the nonlinear specimen response during loading.

Average values of $G_{IIIc}^{CC}(NL)$ and $G_{IIIc}^{CC}(max$ are presented in the column chart in Fig. 12b. Values of G_{IIc} for S2/8552 [21] are also contained in the chart. Again, the mode II value is an average of only three data points. The results show that $G_{IIIc}^{CC}(max$ is much greater than G_{IIc} . Furthermore, the average of $G_{IIIc}^{CC}(NL)$ is 20% lower than G_{IIc} , suggesting that the $G_{IIIc}^{CC}(NL)$ values may not be representative of G_{IIIc} .

X-Radiograph Imaging

Figure 13a contains X-radiographs taken of the two carbon/epoxy ECT specimens (Specimens A and B) that were loaded to a level between P_c^{NL} and P_c^{max} . The load-displacement response of both specimens is shown below the X-radiographs in Fig. 13b. Regression analysis was used to extrapolate the linear portion of the load-displacement responses, and the method detailed in Appendix A was used to determine the values of P_c^{NL} . It is seen that both specimens exhibited some deviation from linearity. The corresponding X-radiographs show that some type of damage initiated from the insert fronts (indicated by the light patches on the surfaces). The damage is likely to consist of delamination and splitting of the 90° plies adjacent to the insert plane. The findings suggest that P_c^{NL} corresponds to the initiation of these energy-absorbing mechanisms. Therefore, the values of $G_{IIIc}^{CC}(max$ and $G_{IIIc}^{LPT}(max$ do not likely correspond to delamination initiation. Additionally, the increase in extent of deviation from linearity with insert length explains the observed dependence of $G_{IIIc}^{CC}(max$ with a/b .

It was observed that the average values of $G_{IIIc}^{CC}(NL)$ for each material was less than the corresponding mode II values. This indicates that the damage observed in the X-radiographs may not constitute initiation of mode III delamination growth. Detailed fractographic analysis is required to confirm this hypothesis.

Discussion

The numerical and experimental results appear to indicate that the fracture data generated from ECT tests on the IM7/8552 and S2/8552 specimens do not correspond to mode III fracture initiation. All specimens exhibited some deviation from linearity, indicating that damage growth may be stable. This was corroborated by the findings from the finite element analysis, showing that the average total strain energy release rate decreases with insert length, Fig. 8.

Data from finite element analyses of the ECT specimens also indicated, that mode III-dominated delamination growth should initiate from the center of the specimens.

X-radiograph images taken of specimens loaded between P_c^{NL} and P_c^{max} indicated that some damage takes place before the maximum test load, P_c^{max} , is reached. Detailed fractographic analyses of the specimen failure surfaces is needed to identify the type of damage revealed by the X-radiographs.

In summary, from the results of studies conducted in the present work, the current data reduction schemes may not be suitable for calculating critical mode III strain energy release rate. Furthermore, detailed inspection of the specimen failure surfaces is required to determine whether mode III delamination was initiated in the specimens.

Concluding Remarks

Edge crack torsion tests were conducted on specimens manufactured from IM7/8552 and S2/8552 tape laminates. In most instances, failure was indicated by a sudden drop in load on the load-displacement response. Two data reduction schemes (compliance calibration and laminated plate theory) were used to calculate perceived critical mode III strain energy release rates. Values calculated using the maximum test load ($G_{IIIc}^{CC}(max)$) exhibited significant dependence on specimen insert length. As the values are meant to represent fracture initiation, the dependence of $G_{IIIc}^{CC}(max)$ with a/b should not be present. It was therefore concluded that the values do not represent initiation of mode III delamination growth. The $G_{IIIc}^{CC}(NL)$ values were moderately insensitive to a/b , however, the average value was less than the average mode II value measured in previous work [21]. This implied that these values also may not reflect initiation of mode III delamination growth.

Two IM7/8552 specimens both with normalized insert lengths of 0.3 were tested. The specimens were loaded to a level above P_c^{NL} but were not allowed to fail (load did not reach P_c^{max}). X-radiograph images of the specimens revealed that damage took place. The observed deviation from linearity of the specimen load-displacement responses suggest the damage growth was stable. This was supported by the findings from the finite element analyses, that average total strain energy release rate decreases with insert length for a constant specimen displacement. The analyses also indicated that specimens should exhibit mode III dominated delamination growth about the specimen center. Detailed inspection of the specimen failure surfaces is required to confirm the numerical analysis findings. This is also necessary to identify the appropriate data reduction strategies if delamination growth is found to be mode III dominated.

References

1. Pipes, R. B., and Pagano, N. J., "Interlaminar Stresses in Composite Laminates Under Uniform Axial Extension," *Journal of Composite Materials*, Vol. 4, 1970, pp.538-548.
2. ASTM D5528-01 "Standard Test Method for Mode I Interlaminar Fracture Toughness of Unidirectional Fiber-Reinforced Polymer Matrix Composites," *2004 Annual Book of ASTM Standards*, Vol.15.03.
3. ASTM D6671M-04 "Standard Test Method for Mixed Mode I-Mode II Interlaminar Fracture Toughness of Unidirectional Fiber-Reinforced Polymer Matrix Composites," *2004 Annual Book of ASTM Standards*, Vol.15.03.
4. Martin, R. H., and Davidson, B. D., "Mode II Fracture Toughness Evaluation Using a Four Point Bend End-Notch Flexure Test," *Plastics, Rubber and Composites*, Vol.28, No.8, 1999, pp.401-406.
5. Vinciguerra, A. J., and Davidson, B. D., "Effect of Crack Length Measurement Technique and Data Reduction Procedures on the Perceived Toughness from Four-Point Bend End-Notch Flexure Tests," *Proceedings of the Seventeenth Annual American Society for Composites Technical Conference*, C. T. Sun and H. Kim, Eds., CRC Press, 2002.
6. Donaldson, S. L., Mall, S., and Lingg, C., "The Split Cantilever Beam Test for Characterizing Mode III Fracture Toughness," *Journal of Composites Technology and Research, JCTRER*, Vol.13, No.1, 1991, pp.41-47.
7. Becht, G., and Gillespie, J. W. Jr, "Design and Analysis of the Crack Rail Shear Specimen for Mode III Interlaminar Fracture," *Composites Science and Technology*, Vol.31, No.2, pp.143-157.
8. Farshad, M., and Flueller, P., "Investigation of Mode III Fracture Toughness Using an Anti-Clastic Plate Bending method," *Engineering Fracture Mechanics*, Vol.60, No.5-6, 1998, pp.597-603.
9. Lee, S. M., "An Edge Crack Torsion Method for Mode III Delamination Fracture Testing," *Journal of Composites Technology and Research, JCTRER*, Vol.15, No.3, 1993, pp.193-201.
10. Li, J., and O'Brien, T. K., "Simplified Data Reduction methods for the ECT Test for Mode III Interlaminar Fracture Toughness," *Journal of Composites Technology and Research, JCTRER*, Vol.18, No.1, 1996, pp.96-101.
11. Li, J., and O'Brien, T. K., "Analytical Investigation of the Hygrothermal Effects and Parametric Study of the Edge Crack Torsion (ECT) Mode III test lay-Ups," *Composite Materials: Fatigue and Fracture, Sixth Volume, ASTM STP 1285*. E. A. Armanios, Ed., ASTM 1997, pp.411-433.
12. Minutes of Sub-Committee D30.06 on Interlaminar Properties. Report from the First Round-Robin on the Edge Crack Torsion Test. May 1997.

13. Minutes of Sub-Committee D30.06 on Interlaminar Properties. Report from the Second Round-Robin on the Edge Crack Torsion Test. May 1999.
14. Krueger, R., and O'Brien, T.K., "A Shell/3D Modeling Technique for the Analysis of Delaminated Composite Laminates," *Composites Part A: Applied Science and Manufacturing*, vol.32, 2001, pp.25-44.
15. O'Brien, T. K., and Krueger, R., "Analysis of Flexure Tests for Transverse Tensile Strength Characterization of Unidirectional Composites," *Journal of Composites Technology and Research*, vol. 25, 2003, pp. 50-68.
16. Irwin, G. R., "Analysis of Stresses and Strains Near the End of a Crack traversing a Plate," *Engineering Journal of Applied Mechanics*, Vol. 24, 1957, pp.361-364.
17. Krueger, R., "Virtual Crack Closure Technique: History, Approach, and Application," *Applied Mechanics Reviews*, Vol.57, No.2, 2004, pp.109-143.
18. Shivakumar, K. N., Tan, P. W., and Newman, J. C., "A Virtual Crack-Closure Technique for Calculating Stress Intensity Factors for Cracked Three Dimensional Bodies," *International Journal of Fracture*, Vol. 36, 1988, pp. R43-R50.
19. Li, J., Lee, S. M., Lee, E. W., and O'Brien, T. K., "Evaluation of the Edge Crack Torsion (ECT) Test for Mode III Interlaminar Fracture Toughness of Laminated Composites. *Journal of Composites Technology and Research, JCTRER*, Vol.19, No.3, 1997, pp.174-183.
20. Li, X., Carlsson, L. A., and Davies, P., "Influence of Fiber Volume Fraction on Mode III Interlaminar Fracture Toughness of Glass/Epoxy Composites," *Composites Science and Technology*, Vol.64, 2004, pp.1279-1286.
21. Hansen, P., and Martin, R., "DCB, 4ENF and MMB Delamination Characterisation of S2/8552 and IM7/8552," Technical Report N68171-98-M-5177, Materials Engineering Research Laboratory Ltd. (MERL), Hertford, U.K., 1999.

Appendix A

Calculating Load at Deviation from Linearity

The load-displacement response from an ECT test on a glass/epoxy specimen with a normalized insert length of 0.2 is shown in Fig. A1. The response is initially nonlinear, corresponding to seating of the load and support pins on the ECT specimen. This is proceeded by a linear section, corresponding to the elastic response of the specimen. At some load, P_c^{NL} , the response begins to deviate from linearity until a maximum load is reached, followed by a sudden load drop, indicating specimen failure. A linear regression analysis is performed to estimate the linear fit corresponding to the linear portion of the load-displacement response (load range bounded by broken lines in Fig. A1). The load is calculated using the linear fit over the entire displacement range of the load-displacement response. A plot of this linear fit load, P_{LR} , is superimposed onto the original load-displacement plot in Fig. A1. The difference between the linear fit load and the original experimental load ($P_{LR}-P_{EXP}$) is plotted as a function of displacement, as shown in Fig. A2. The onset of deviation from linearity was then determined by recording the displacement value after which the linear regression and experimental load values begin to diverge, as shown in Figure A2. The load at deviation from linearity, P_c^{NL} , is then found from the original load-displacement plot, as illustrated in Fig. A1.

TABLE 1. MATERIAL PROPERTIES [15].

S2/8552 Unidirectional Glass-Epoxy Prepreg		
$E_{11} = 47.71 \text{ GPa}$	$E_{22} = 12.27 \text{ GPa}$	$E_{33} = 12.27 \text{ GPa}$
$\nu_{12} = 0.278$	$\nu_{13} = 0.278$	$\nu_{23} = 0.403$
$G_{12} = 4.83 \text{ GPa}$	$G_{13} = 4.83 \text{ GPa}$	$G_{23} = 4.48 \text{ GPa}$
IM7/8552 Unidirectional Carbon-Epoxy Prepreg		
$E_{11} = 161.0 \text{ GPa}$	$E_{22} = 11.38 \text{ GPa}$	$E_{33} = 11.38 \text{ GPa}$
$\nu_{12} = 0.32$	$\nu_{13} = 0.32$	$\nu_{23} = 0.436$
$G_{12} = 5.17 \text{ GPa}$	$G_{13} = 5.17 \text{ GPa}$	$G_{23} = 3.98 \text{ GPa}$

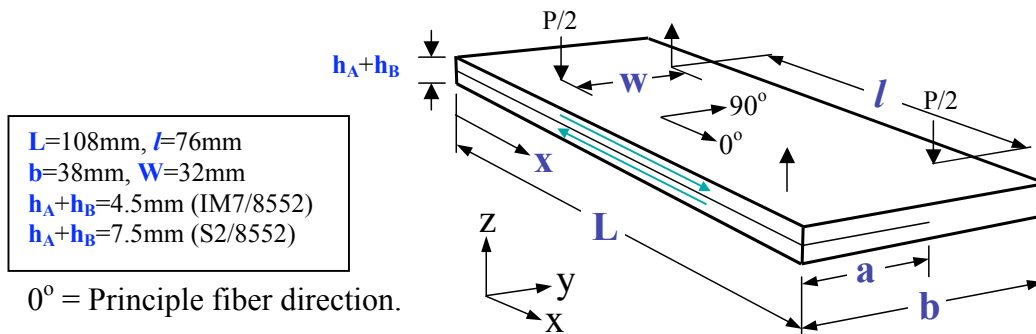


FIGURE 1. Schematic of ECT specimen.

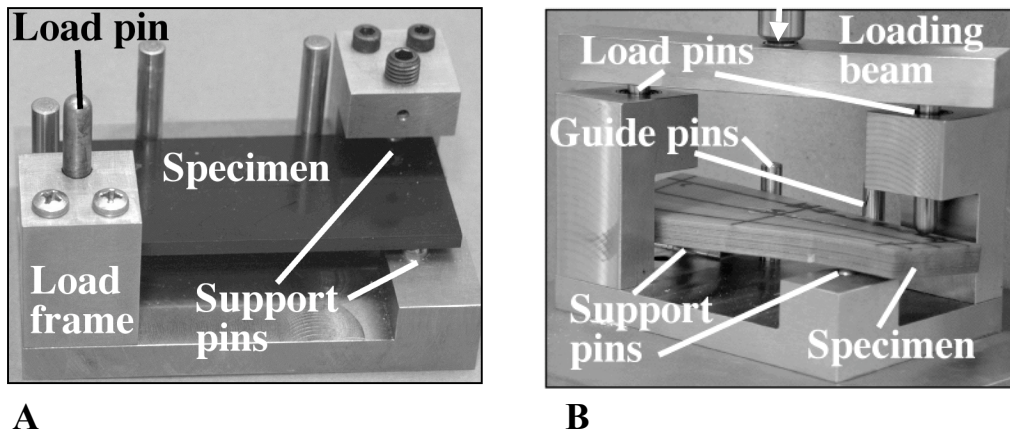


FIGURE 2. (a) Original ECT test fixture. (b) Current ECT test fixture (showing deformed specimen).

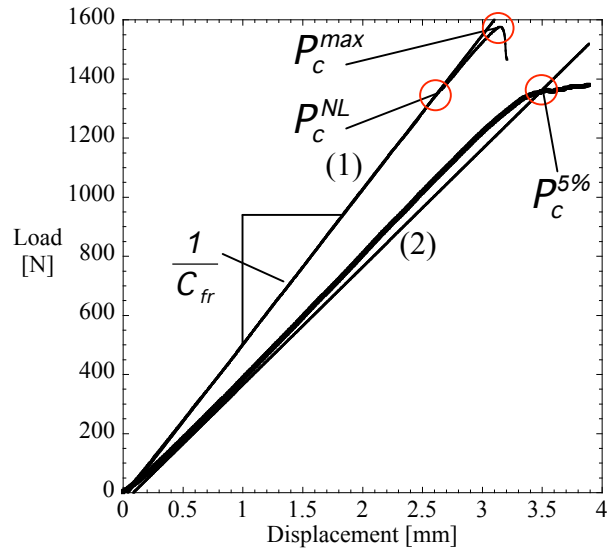


FIGURE 3. Example load displacement responses from ECT tests.

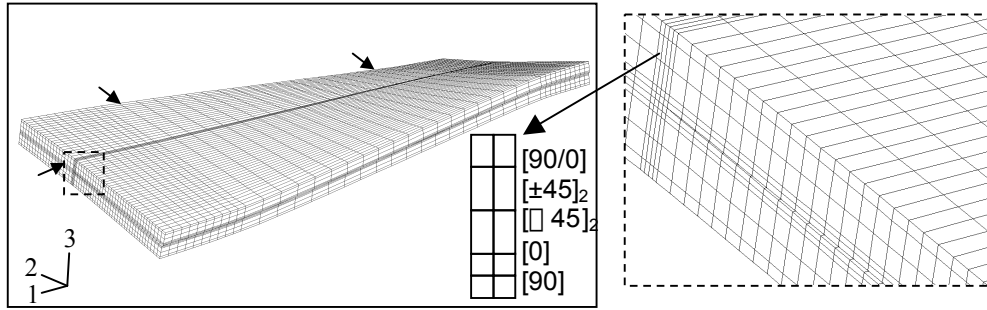


FIGURE 4. Finite element mesh of IM7/8552 ECT specimen with $a/b=0.6$.

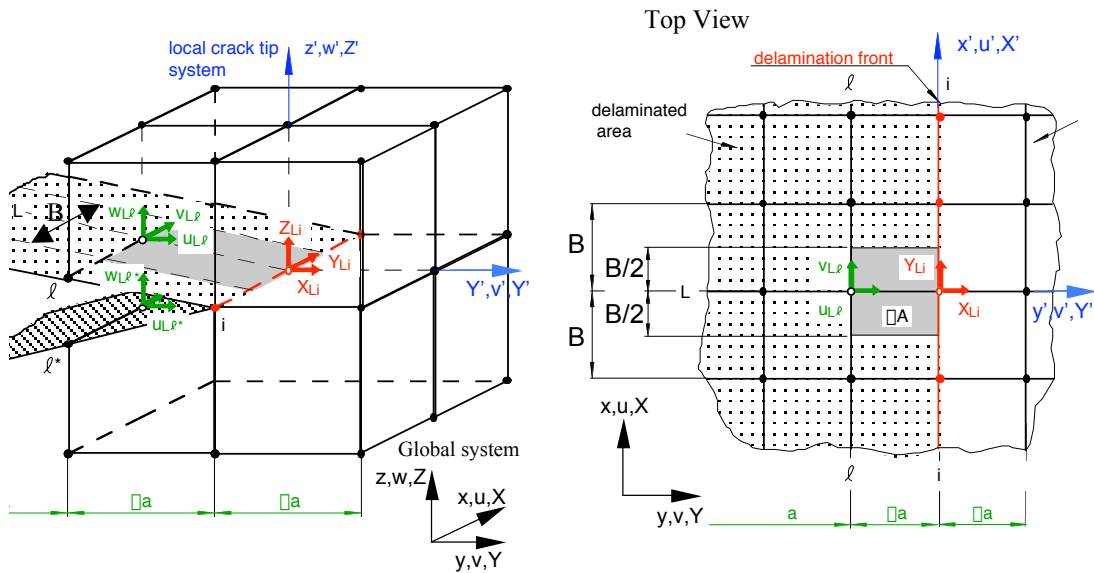


FIGURE 5. Delamination front region of finite element models.

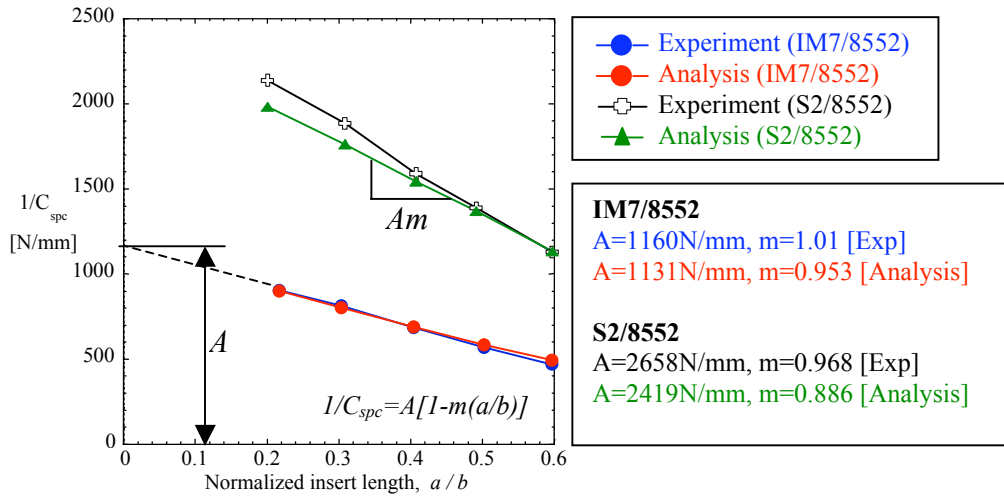


FIGURE 6. Specimen stiffness versus a/b . Comparison of experiment and analysis.

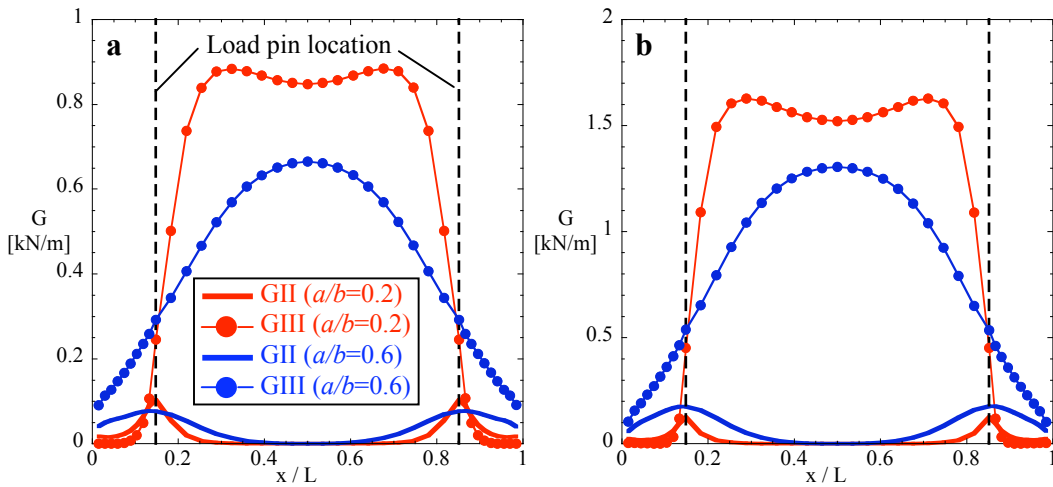


FIGURE 7. Computed strain energy release rate distribution across delamination front (a) IM7/8552 specimens, (b) S2/8552 specimens.

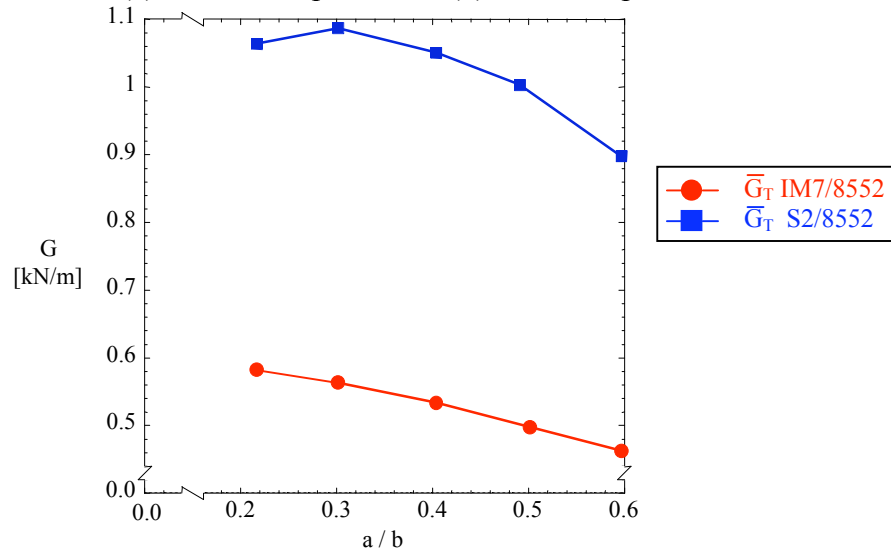


FIGURE 8. Computed average total strain energy release rate versus a/b .

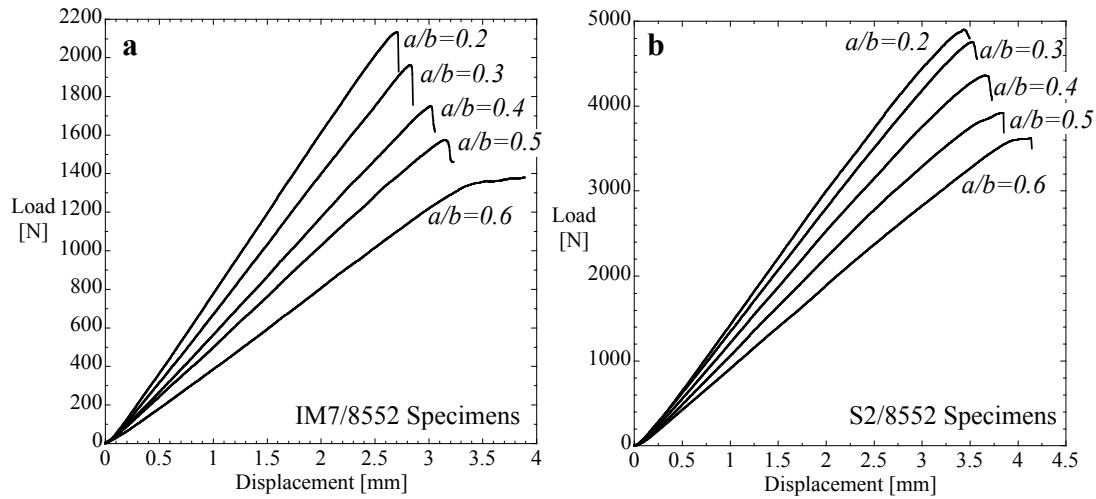


FIGURE 9. Load-displacement responses from ECT tests (a) IM7/8552 specimens, (b) S2/8552 specimens.

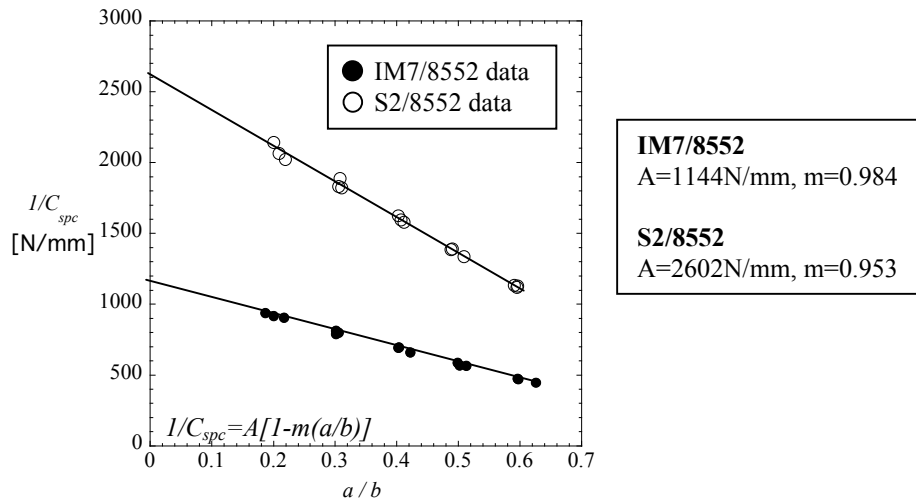


FIGURE 10. Stiffness versus a/b from ECT tests.

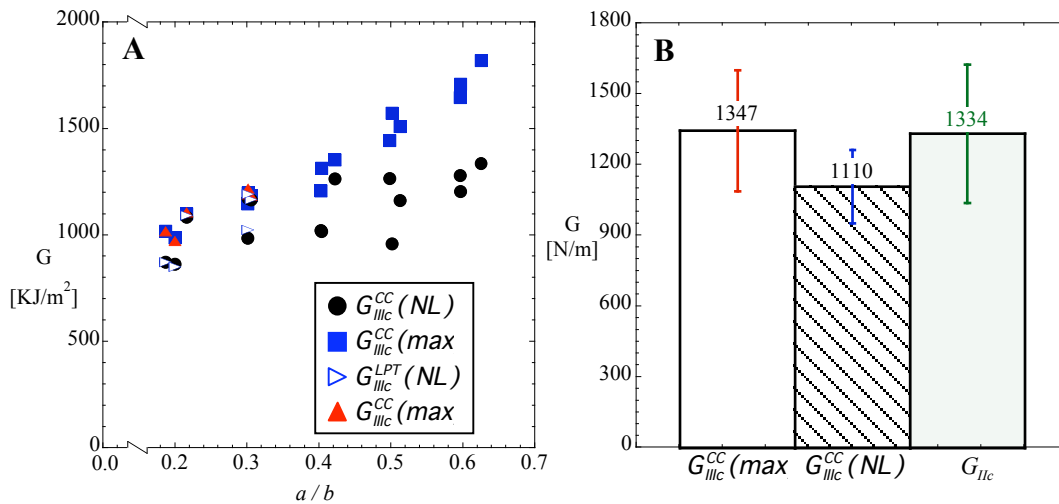


FIGURE 11 (a) Perceived critical mode III strain energy release rate versus insert length of IM7/8552. (b) Average perceived critical strain energy release rate values.

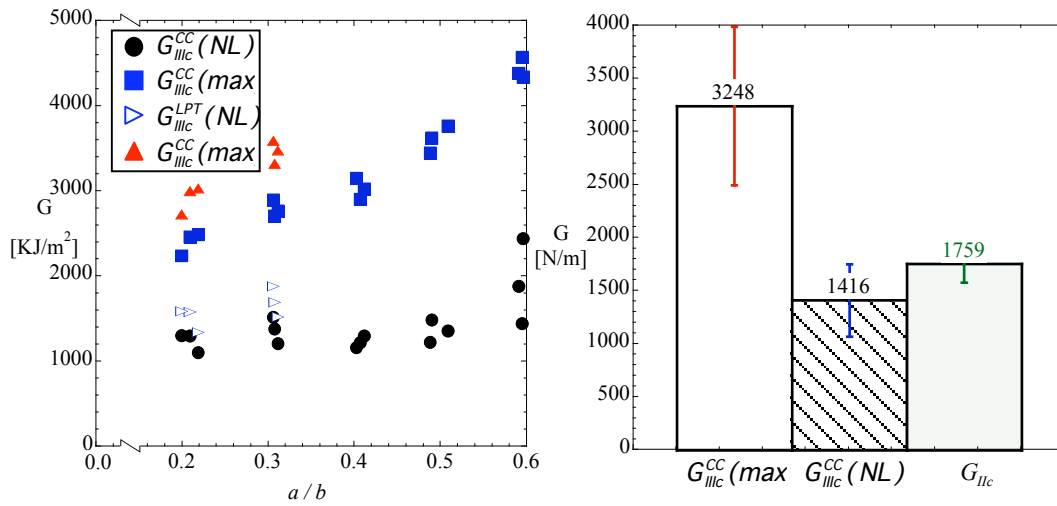


FIGURE 12 (a) Perceived critical mode III strain energy release rate versus insert length of S2/8552. (b) Average perceived critical strain energy release rate values.

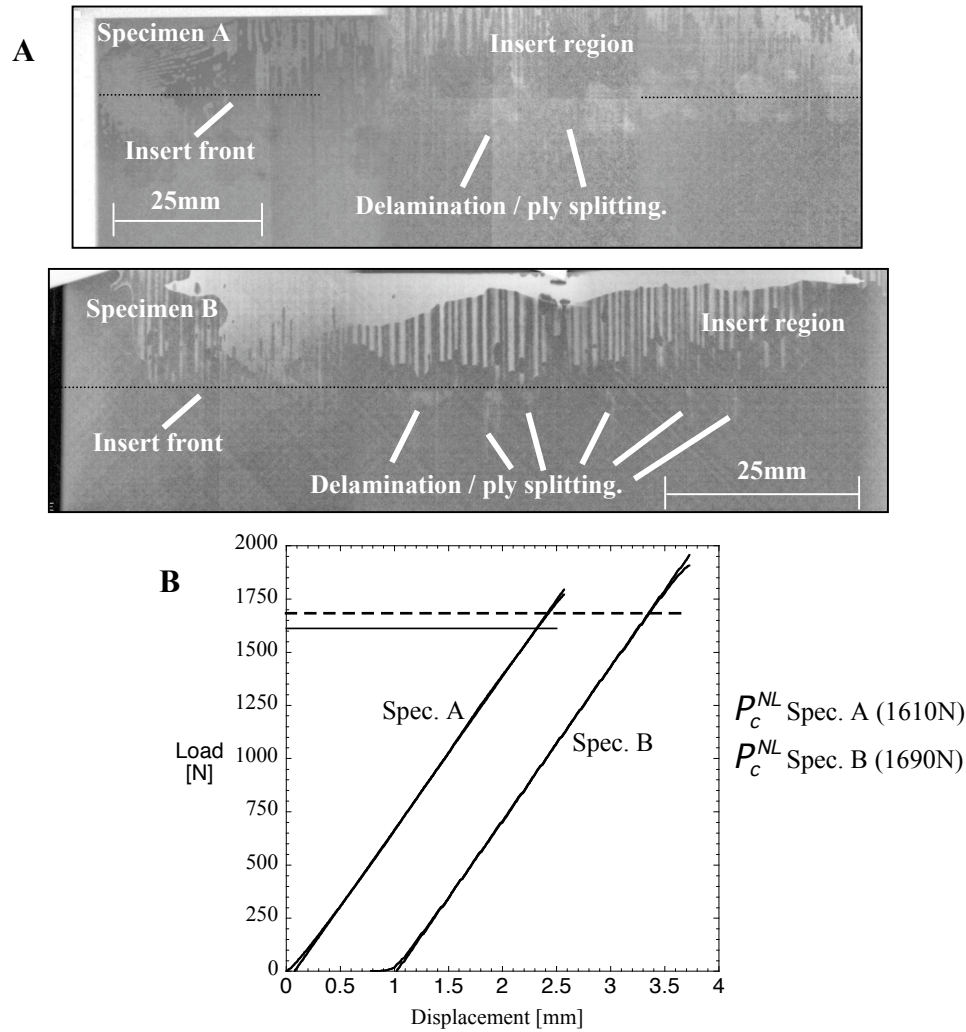


FIGURE 13 (a) X-radiographs of IM7/8552 specimens. (b) Load displacement response of the specimens.

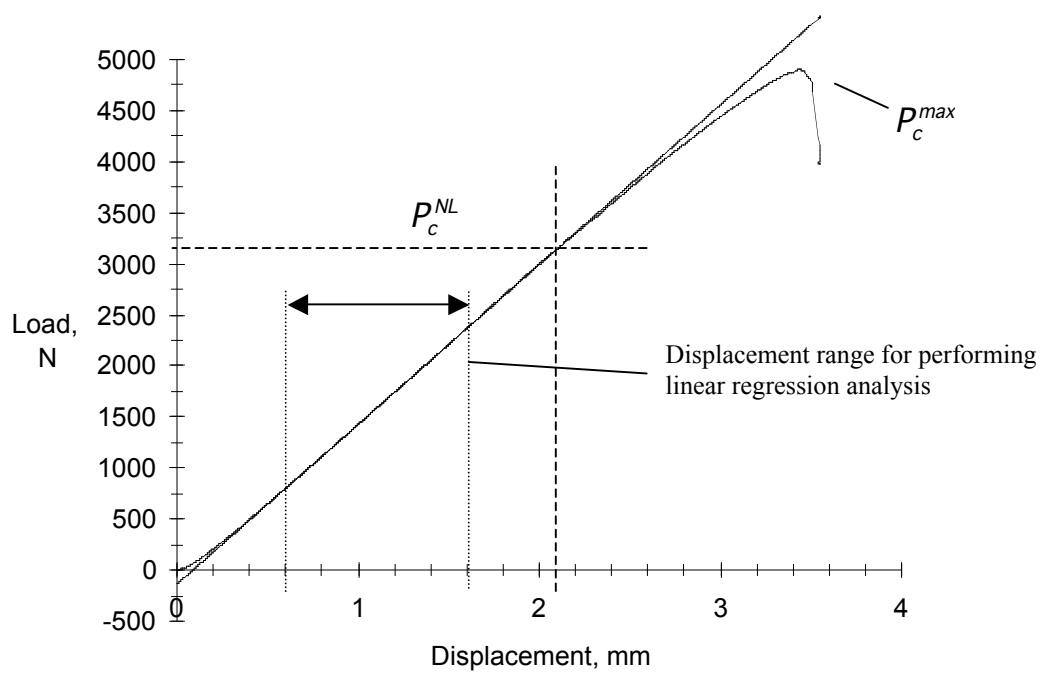


FIGURE A1. Load-displacement response typical from an ECT test.

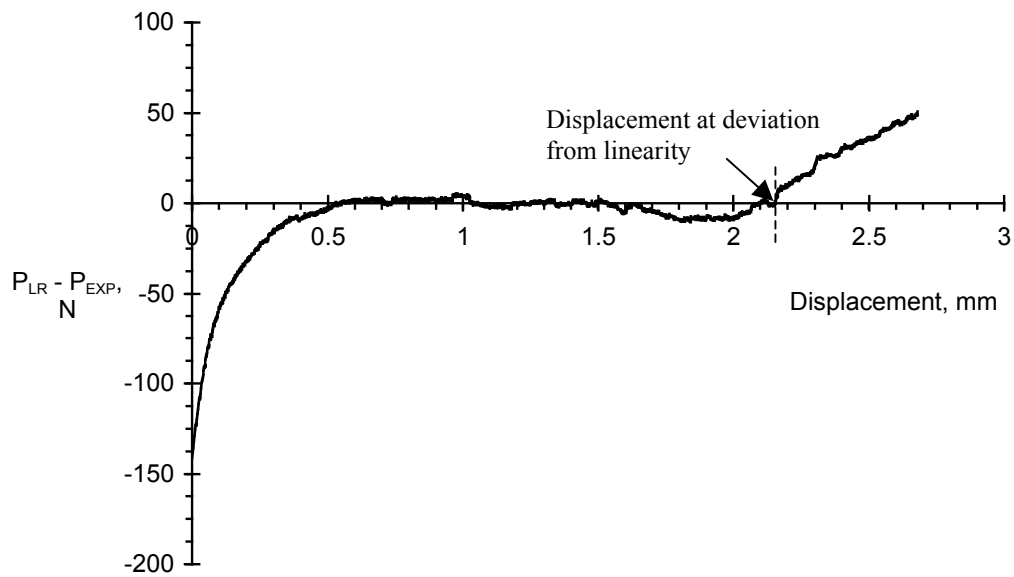


FIGURE A2. Difference between P_{LR} and P_{EXP} versus displacement.